2022

The Experimental Study of Defrosting Energy of an Air-source Heat Pump System Under Various Conditions

Wenying Zhang

Pega Hrnjak

An Experimental Study of Defrosting Energy of an R744 Automobile Air-Source Heat Pump System with Different Defrost-Initiation Criteria

Wenying ZHANG [1], Pega HRNJAK[1, 2]*

[1]ACRC, University of Illinois, Urbana, Illinois, USA
wenying3@illinois.edu
[2]Creative Thermal Solutions, Inc., Urbana, Illinois, USA
pega@illinois.edu
* Corresponding Author

ABSTRACT

This paper analyzes the energy supplied for defrosting and its consumption. Data are obtained in experiments using a transcritical R744 heat pump system in the outdoor condition of 0℃ and 90% RH. Defrosting was conducted by reversing the flow to warm the outdoor coil and melt the accumulated frost. The effects of the criterion for initiation of defrosting on the defrost energy flow during continuous frosting/defrosting cycles are presented. Also, the distribution of retained meltwater on the outdoor microchannel heat exchanger is firstly reported in the open literature. The results show that it costs less energy per operating time to defrost when applying 10 times instead of 5 times the initial DP_{ea} as the defrost-initiation criterion. The data show less even frost distribution as the number of defrosting cycles increases, which can cause more heat loss to the ambient and reduce the defrosting efficiency.

1. INTRODUCTION

In recent decades, electric vehicles (EVs) have been promoted in many countries to reduce air pollution and limit climate change. Despite the rapid growth of the EV market, EVs still face the challenge of range anxiety. Reversing the operation of Air-Conditioning (AC) system and using the Heat Pump (HP) function can help mitigate that problem. In that case, issues related to frosting, defrosting, and condensate removal for the outdoor microchannel evaporator become important. Frost grows on the outdoor microchannel evaporator when the surface temperature of it is lower than both the freezing point of water and the dew point temperature during the operation. The engineering defrosting methods can be divided into two major categories: passive methods and active methods.

Even the passive methods have the potential to delay the frost accumulation on the outdoor coil, the frost that is built after the delay should be removed by active methods periodically for better system performance. Among the active defrosting methods, the reverse cycle is the most widely studied due to its fast action, relatively low initial cost, and easy control. Payne and O'Neal (1995) experimentally studied the frost accumulation and defrost cycle of a 10.6 kW air-source residential heat pump with the original scroll compressor and a reciprocating compressor. The defrosting was conducted by reversing the cycle when the heating capacity drops by 20% and terminated when the temperature of the lowest liquid line of the outdoor coil reached 26.7℃. The results showed that the low-efficient reciprocating compressor produced 18% higher discharge superheat and thus defrost 5% faster than the scroll compressor with a similar capacity. Huang et al. (2009) investigated and compared the dynamic characteristics of Reverse-Cycle Defrosting (RCD) and Hot Gas Bypass Defrosting (HGBD) using a 55-kW air source water heater heat pump. The results showed that the water temperature has a smaller fluctuation for the HGBD method. However, HGBD requires 2.89 times the defrosting time required by RCD. Also, the suction and discharge superheat of HGBD is lower than those of RCD. This might reduce the cyclic efficiency of the heat pump system, which was not discussed in this paper. Dong et al. (2012) conducted experiments to study the defrosting energy supplies and consumptions during a reverse cycle defrosting of an R22 residential air-source heat pump with tube-and-fin heat exchangers. The indoor air provided 71.8% of the total heat supplied for defrosting, of which 59.4% was used for melting frost. Also, the maximum defrosting efficiency (energy required to melt the frost and vaporize the retained melted frost/ energy supplied to the outdoor coil) could be up to 60.1%. However, only one group of data under one operating condition with tube-and-fin heat exchangers was provided in this paper and the effects of the many other control parameters, like the control strategy of defrosting and the periodic performance, were not included. Song et al. (2017) further explored the energy transfer in a residential ASHP during defrosting by studying the effects of different outdoor coil sizes. It is reported that the defrosting efficiency was improved from 42.26% to 48.34% when the outdoor coil is enlarged by 50%.

Although reverse cycle defrosting has been widely studied and applied for residential ASHP systems with tube-fin heat exchangers, the studies for automobile ASHP systems with microchannel heat exchangers are relatively rare. Steiner and Rieberer (2013) investigated the defrosting performance of an automobile CO_2 heat pump system both experimentally and numerically. The data showed that the defrosting took less than 2 minutes with reverse cycle defrosting, and the final refrigerant inlet temperature of the outdoor coil reached 50°C. The transient simulation results indicate that there is an optimal throttle opening regarding defrosting time and efficiency for the test conditions. Zhang and Hrnjak (2021) experimentally studied the effects of different defrost-start criteria on the efficiency and frost accumulation of an automobile CO_2 heat pump during periodic frosting and reverse-cycle defrosting. The heating capacity and efficiency of the HP drop less than 10% when the air-side pressure drop reaches 5 times the initial value. Also, the frosting time increases from 28 to 64 minutes and the defrosting time drops from 7.2% to 5.7%, when the criterion changes from 5 to 10 times of the initial air-side pressure drop. However, the defrosting efficiency and the energy analysis during the defrosting are not well studied for automobile heat pump systems using microchannel heat exchangers.

In this paper, we investigate the effects of the defrost-initiation criterion on the defrosting efficiency and the energy flow during several continuous defrosting cycles using a reversible automobile CO_2 heat pump. The transient process of the frost growth and the melting of the frost were monitored using web cameras. The frost accumulation, meltwater retention, and drainage were measured and calculated. The energy supply and consumption of continuous defrosting processes were discussed and analyzed.

2. EXPERIMENTAL SETUP

2.1 Facility

A reversible CO_2 heat pump system was used for continuous frosting/defrosting experiments. The schematics of the heat pump system, the geometry of the key components, as well as the details of the sensors were reported in our previous paper (Zhang and Hrnjak, 2021). In that paper, we focused on the effects of the defrost-initiation criteria on the heating performance, while we investigate the defrosting efficiency and energy flow during the defrosting process in this paper.

2.2 Experimental procedure of defrosting process

The overall experimental procedures of continuous frosting/defrosting experiments were presented in our previous paper (Zhang and Hrnjak, 2021). Table 1 shows the operating conditions of the frosting/defrosting experiments in this paper.

Table 1: Operating conditions of frosting/defrosting experiments

Microchannel tube orientation	$T_{OD,eai}$ [°C]	$RH_{OD,ei}$ [%]	$V_{OD,eai,ini}$ [m/s]	$T_{ID,cai}$ [°C]	$U_{ID,cai}$ [kg/min]	# of frosting cycles	Defrost initiation criterion	Defrost stop criterion
Vertical	0	90	3.0	20	7.0	1 to 3	5× $DP_{ea,ini}$	$T_{OD,cro}$ = 45 °C
						1 to 2	10× $DP_{ea,ini}$	

2.3 Data reduction of the transient performance of the defrost of the HP system

During the defrosting process, the cooling capacity of the indoor coil was calculated using air-side measurements, following (1)

$$Q_{ID,e,air} = \dot{m}_{ID,dryair}(h_{ID,eai} - h_{ID,eao}) \quad \textbf{(1)}$$

Where the airflow rate $\dot{m}_{ID,dryair}$ was calculated using the measured air temperature $T_{ID,ean}$, dew point $T_{ID,dpen}$, and pressure drop $DP_{ID,en}$ at the indoor nozzles. The enthalpies of air $h_{ID,eai}$ and $h_{ID,eao}$ were determined using air temperatures and dew points at the indoor coil inlet ($T_{ID,eai}$ and $T_{ID,dpei}$) and indoor nozzles' exits ($T_{ID,ean}$ and $T_{ID,dpen}$). On the other hand, the heating capacity of the outdoor coil can be only calculated using the refrigerant-side measurements:

$$Q_{OD,c,ref} = (1-OCR)\dot{m}_r(h_{OD,cri} - h_{OD,cro}) + OCR \cdot \dot{m}_r(h_{OD,coi} - h_{OD,coo}) \quad \textbf{(2)}$$

Where OCR is measured by the oil sampler installed across the mass flow meter on the liquid line. In this paper, the

OCR is measured to be 2%. $\dot{m}_r$ was measured by the mass flow meter, and it is actually the mass flow rate of POE oil and CO_2 mixture. The refrigerant enthalpies $h_{OD,cri}$ and $h_{OD,cro}$, oil enthalpies $h_{OD,coi}$ and $h_{OD,coo}$ were determined from the pressures and temperatures measured at outdoor condenser/ gas cooler inlet ($T_{OD,cri}$ and $P_{OD,cri}$) and outlet ($T_{OD,cri}$ and $P_{OD,cri}$).

Like the heating capacity of the outdoor condenser/gas cooler, the heating capacity of IHX was calculated using the refrigerant properties in the high-pressure side, following equation(3):

$$Q_{IHX,high} = (1-OCR)\dot{m}_r(h_{OD,cro} - h_{ID,xri}) + OCR \cdot \dot{m}_r(h_{OD,coo} - h_{ID,xoi}) \quad \textbf{(3)}$$

Where the refrigerant and oil enthalpy ($h_{ID,xri}$ and $h_{ID,xoi}$) were determined using the pressure and temperature measured at the inlet of the expansion valve used in defrosting/AC mode. Also, the cooling capacity of the low-pressure side of the IHX equals the heating capacity, assuming there is no heat loss to the ambient through the insulation. Thus, we can determine the state of the refrigerant at the accumulator exit based on the low-pressure side of the IHX.

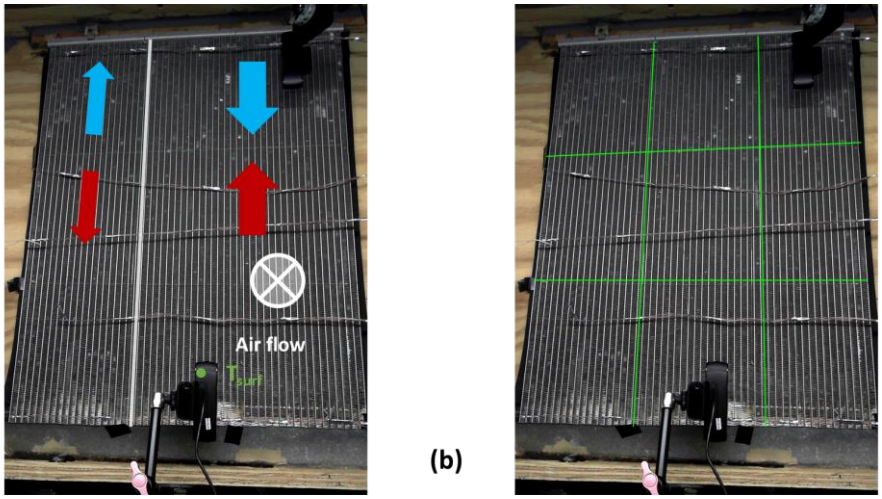

The flow directions of refrigerant and air: **blue**- evaporator in HP mode; **red**- condenser in defrosting mode; **white**- airflow in HP mode

The meltwater was collected from the outdoor coil separately for 9 blocks

Figure 1: The vertically oriented outdoor coil used in frosting/defrosting experiments (17 and 34 tubes for the left and right pass; **green spot**- the thermocouple used to measure surface temperature T_{surf})

Finally, to collect the meltwater retained on the outdoor coil, we switched off the compressor, heaters, steam line, and blowers. Then, we collected the retained water $M_{retained}$ on the outdoor coil using compressed air and paper towels placed exactly on each of the blocks (Fig. 1 (b)). Also, we collected the drained water $M_{drained}$ from the pan installed below the coil with a hose and a 500 mL beaker. The difference between the total amount of accumulated frost and the sum of retained water and drained water was considered as the mass of water vaporized during the defrosting process, following:

$$M_{vaporized} = M_{frost} - M_{retained} - M_{drained} \quad \textbf{(4)}$$

Where, M_{frost} is the integrated total mass of frost accumulated on the outdoor coil over the frosting cycle (Zhang and Hrnjak, 2021).

2.4 Data reduction of the energy supply during defrosting

There were three major energy supplies during the defrosting: the heat from indoor warm coil metal, the heat from indoor 20°C warm air, and energy from the compressor power. The heat supplied by the indoor air was calculated by integrating $Q_{ID,e,air}$ over the defrosting time $t_{defrosting}$, as shown in equation (5)

$$E_{ID,e,air} = \int_0^{t_{defrosting}} Q_{ID,e,air}\, dt \quad \textbf{(5)}$$

The heat supplied by the indoor coil metal can be calculated using the initial and final average temperatures of the indoor evaporator during the defrosting, as shown in (6):

$$E_{ID,e,coil} = M_{ID,coil} cp_{al} \left[ave\left(T_{ID,cri}, T_{ID,cro}\right)_{frost,\,final} - \left(\frac{T_{ID,eri} + T_{ID,ero}}{2} \right)_{defrost,\,final} \right] \quad \textbf{(6)}$$

Where, $M_{ID,\,coil}$ is the mass of the indoor aluminum coil. cp_{al} is the specific heat of aluminum. $T_{ID,cri}$ and $T_{ID,cro}$ are the refrigerant inlet and exit temperatures of the indoor gas cooler during the last frosting cycle. Also, the $ave(T_{ID,\,cri}, T_{ID,cro})$ represents the calculation of the average coil temperature following a logarithmic temperature profile along the flow direction, while using $T_{ID,\,cri}$ and $T_{ID,cro}$ as the starting and ending points. The subscripts *frost,final* represents the final states of the previous frosting cycle, and *defrost,final* represents the final states of the current defrosting cycle. Also, the transient capacity of the heat supply by the indoor warm coil $Q_{ID,e,coil}$ can be calculated as the derivative of $E_{ID,e,coil}$ with respect to time.

The compressor power W_{comp} during defrosting was directly measured by a watt transducer, and the energy supplied by the compressor was calculated following:

$$E_{comp,defrost} = \int_0^{t_{defrosting}} W_{comp}\, dt \quad \textbf{(7)}$$

The total energy supplied for defrosting $E_{total,supply}$ was calculated by adding the three terms together:

$$E_{total,\,supply} = E_{ID,e,air} + E_{ID,e,coil} + E_{comp,defrost} \quad \textbf{(8)}$$

2.5 Data reduction of the energy consumption during defrosting

The energy consumption is divided into four parts: the heat used to warm up the cold outdoor coil metal, the heat used to preheat the frost to 0°C and to melt the frost, the heat used to warm and vaporize the meltwater during the defrosting and drainage, and the heat loss to the cold ambient air. First, the total amount of all four parts of energy consumption was calculated by integrating $Q_{OD,c,ref}$ over the defrosting time $t_{defrosting}$ using equation (9):

$$E_{OD,c,ref} = \int_0^{t_{defrosting}} Q_{OD,c,ref}\, dt \quad \textbf{(9)}$$

The energy used to warm the cold metal of the outdoor coil was calculated using equation (10):

$$E_{OD,c,coil} = M_{OD,coil} cp_{al} \left(\left(\frac{T_{OD,cri} + T_{OD,cro}}{2} \right)_{defrost,\,final} - \left(\frac{T_{OD,eri} + T_{OD,ero}}{2} \right)_{frost,\,final} \right) \quad \textbf{(10)}$$

Where, $M_{OD,coil}$ is the mass of the outdoor coil. $T_{OD,cri}$ and $T_{OD,cro}$ are the refrigerant inlet and exit temperatures of the outdoor coil/condenser at the *final* stage of the current *defrosting* cycle. $T_{OD,eri}$ and $T_{OD,ero}$ are the refrigerant inlet and exit temperatures of the outdoor coil/evaporator at the *final* stage of the previous *frosting* cycle. Similarly, the transient heating load of heating the metal of outdoor coil $Q_{OD,c,coil}$ can be calculated as the derivative of $E_{OD,c,coil}$ with respect to time.

The energy used to preheat and melt the frost $E_{OD,c,frost}$ can be calculated using equation(11):

$$E_{OD,c,\,frost} = M_{frost} cp_{frost} \left(0 - \left(\frac{T_{OD,eri} + T_{OD,ero}}{2} \right)_{frost,\,final} \right) + M_{frost} h_{frost,\,fusion} \quad \textbf{(11)}$$

Where, cp_{frost} is the specific heat of frost- 2.108 kJ/(kg-K). $T_{OD,eri}$ and $T_{OD,ero}$ are the refrigerant inlet and exit temperatures of the outdoor coil/evaporator at the *final* stage of the last *frosting* cycle. $h_{frost,fusion}$ is the latent heat to melt the frost- 333.5 kJ/kg. The transient heating load of preheating and melting the frost $Q_{OD,c,frost}$ can be calculated as the derivative of $E_{OD,c,frost}$ with respect to time.

The energy used to heat and vaporize the water $E_{OD,c,water}$ was estimated using equation (12):

$$E_{OD,c,water} = M_{drained} cp_{water} (10-0) + M_{retained} cp_{water} \left(\left(\frac{T_{OD,cri} + T_{OD,cro}}{2} \right)_{defrost,\,final} - 0 \right) + M_{vaporized} \left[cp_{water} (50-0) + h_{water,vaporization} \right] \quad (12)$$

Where, cp_{water} is the specific heat of water, and $h_{water,\,vaporization}$ is the latent heat to vaporize water at 50 ℃. In the calculation, the drained water was assumed to leave the outdoor coil at 10℃. The average of the *final* temperature of $T_{OD,cri}$ and $T_{OD,cro}$ is used to represent the final temperature of retained water. The evaporated water was assumed to be heated up to 50 ℃ and then vaporized. It is clear that the accuracy of $E_{OD,c,frost}$ and $E_{OD,c,water}$ in (11) and (12) considerably rely on the accuracy of the mass measurements.

Based on energy conservation, the heat loss to the outdoor ambient air was calculated using equation (13):

$$E_{OD,c,loss} = E_{OD,c,ref} - E_{OD,c,\,frost} - E_{OD,c,coil} - E_{OD,c,water} \quad (13)$$

3. RESULTS AND DISCUSSION

3.1 The overall performance of continuous defrosting cycles

A series of continuous frosting/defrosting experiments were conducted following previously described experimental procedures (Zhang and Hrnjak, 2021), and the data were processed following the equations (1) to (13). Figure 2 presents the accumulated mass of frost and meltwater on the outdoor coil during continuous frosting/defrosting cycles with different defrost-initiation criteria in the outdoor condition of 0℃ and 90% RH.

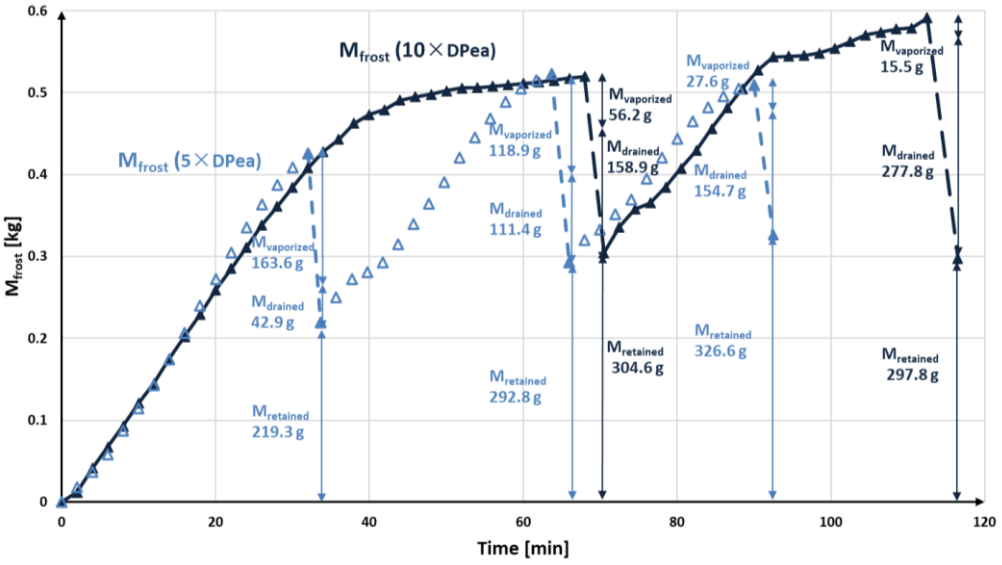

Figure 2: The mass of accumulated frost and meltwater on the outdoor coil during continuous frosting and defrosting cycles at 0℃ and 90% RH

As shown in Figure 2, the defrosting time $t_{defrosting}$ is 1.7, 2.3, and 2.5 minutes for the continuous three defrosting cycles with 5 times the initial DP_{ea} as the defrost-initiation criterion. While it is 2.5 and 4.0 minutes for the continuous two defrosting cycles with 10 times the initial DP_{ea} as the defrost-initiation criterion. Also, the water retention $M_{retained}$ is 219.3 g, 292.8 g, and 326.6 g after continuous three defrosting using 5 times the initial DP_{ea} as the defrost-initiation criterion, and it is 304.6 g and 297.8 g after defrosting using 10 times of the initial DP_{ea} as the defrost-initiation criterion. Overall, the defrosting time and water retention on the outdoor coil increase gradually with the number of the frosting/defrosting cycles. This is due to the retained water turning into ice instead of high-porosity frost at the beginning of the next frosting cycle, so the density of the re-accumulated frost increases near the coil surface. This increases the amount of frost accumulated, the time and energy required to defrost, and the water retention in the next re-frosting cycle. In addition, the final water retention is 326.6 g and 297.8 g for the third defrosting cycle using 5 times of the initial DP_{ea} as the defrost-initiation criterion and for the second defrosting cycle using 10 times of the initial DP_{ea} as the defrost-initiation criterion, respectively. This indicates the retained water

gets saturated with approximately 300 g for the vertically installed outdoor coil. Further refrosting cycles are likely to show repeatable performance.

Similar to the water retention $M_{retained}$, the drained water $M_{drained}$ increases gradually with the number of the frosting/defrosting cycles (Figure 2): it drains 42.9 g, 111.4 g, and 154.7 g for the continuous three defrosting using 5 times of the initial DP_{ea} as the defrost-initiation criterion, and it drains 158.9 g and 277.8 g after defrosting using 10 times of the initial DP_{ea} as the defrost-initiation criterion. On the contrary, the mass of the vaporized water $M_{vaporized}$ reduces from hundreds of grams to tens of grams with the increased number of the frosting/defrosting cycles (Figure 2). This is likely due to the increased thickness of the water film and the reduced surface temperature of the water film in the second or third defrosting cycle. The lower the surface temperature of the water film, the less kinetic energy of the water molecules on the surface. Therefore, less water was vaporized in the second and third defrosting cycles than it was in the first defrosting cycle.

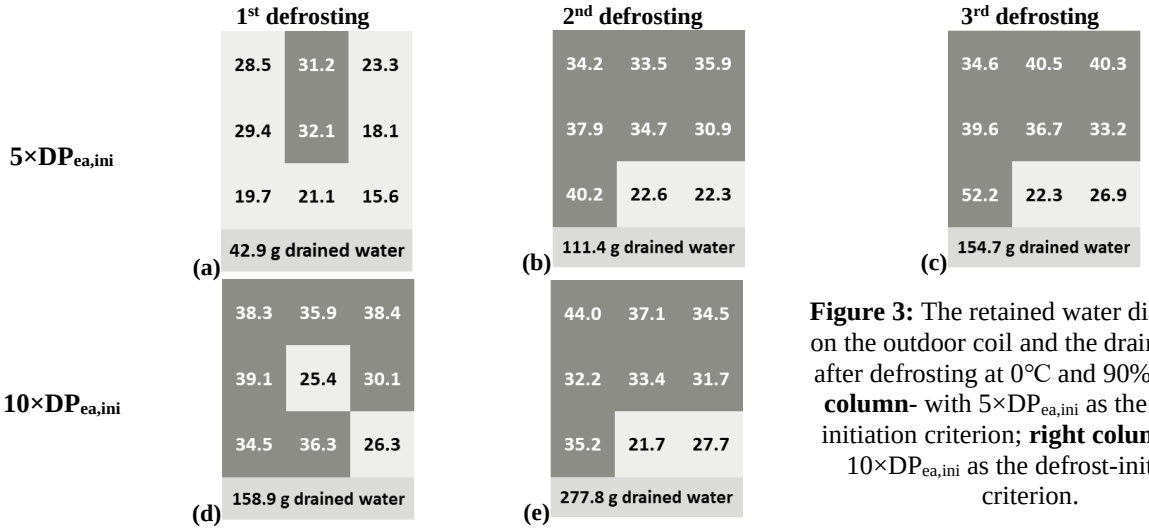

Figure 3: The retained water distribution on the outdoor coil and the drained water after defrosting at 0℃ and 90% RH: **left column**- with $5\times DP_{ea,ini}$ as the defrost-initiation criterion; **right column**- with $10\times DP_{ea,ini}$ as the defrost-initiation criterion.

Figure 3 shows the retained water distribution on the outdoor coil and the drained water after defrosting, and the dark grey color represents the block retaining more than 30 g of water after defrosting. The distribution of retained water matches the frost distribution on the outdoor coil after the first defrosting cycle, as shown in Figure 3(a) and in our previous paper (Figure 7, Zhang and Hrnjak, 2021). Also, the distribution of retained water becomes less even in the following defrosting cycles. On the one hand, the superheated refrigerant enters from the right-bottom of the outdoor coil during the defrosting, and most of the evaporation occurs here. On the other hand, more water drains from the top to the bottom in the left pass, as shown in Figure 3(c). The unevenness of the retained water can increase heat loss to the ambient and reduce the defrosting efficiency and the overall performance of the heat pump system.

3.2 The energy supply during continuous defrosting cycles

Figure 4 presents the transient energy supply capacities of the indoor air $Q_{ID,e,air}$, compressor W_{comp}, indoor coil metal $Q_{ID,e,coil,}$ and the integrated total energy supply ($E_{total,supply}$ in kJ) over the defrosting time with different defrost-initiation criteria in the operating condition of 0℃ and 90% RH for continuous defrosting cycles. The warm indoor coil metal provides most of the defrosting energy at the beginning of the defrosting process- approximately the first half to one minute for different cycles, when the temperature of the indoor coil is higher than the inlet air temperature. This capacity $Q_{ID,e,coil}$ firstly peaks due to the decreasing evaporating temperature, as shown in Figure 5. Then, it reduces to zero as the temperature of the coil approaches the lowest evaporating temperature, which can be as low as -5℃. Finally, $Q_{ID,e,coil}$ stays below zero because the temperatures of both refrigerant and indoor coil metal increase during this start-up process (T_{eri} and T_{ero} in Figure 5), so that the coil metal is warmed up by the indoor air during the latter half of this defrosting process and no longer provides energy for defrosting.

On the other hand, the indoor air supplies most of the energy after the coil temperature approaches the evaporating temperature. After reversing the system and the restart of the compressor, the evaporating temperature first hit the lowest point of approximately -5℃, and then increased and stabilized at 7℃, as shown in Figure 5. As a result, the capacity $Q_{ID,e,air}$ increased to the peak value and then decreased. The power consumption of the compressor W_{comp}

increased gradually from about 1 to 2 kW during the defrosting, as the mass flow rate of refrigerant increased from approximately 20 to 38 g/s. In the meanwhile, the evaporator exit quality drops significantly and the two-phase refrigerant enters the accumulator, so the liquid refrigerant migrates from the cold outdoor coil and liquid line (in previous HP mode) to the accumulator during the short defrosting operation.

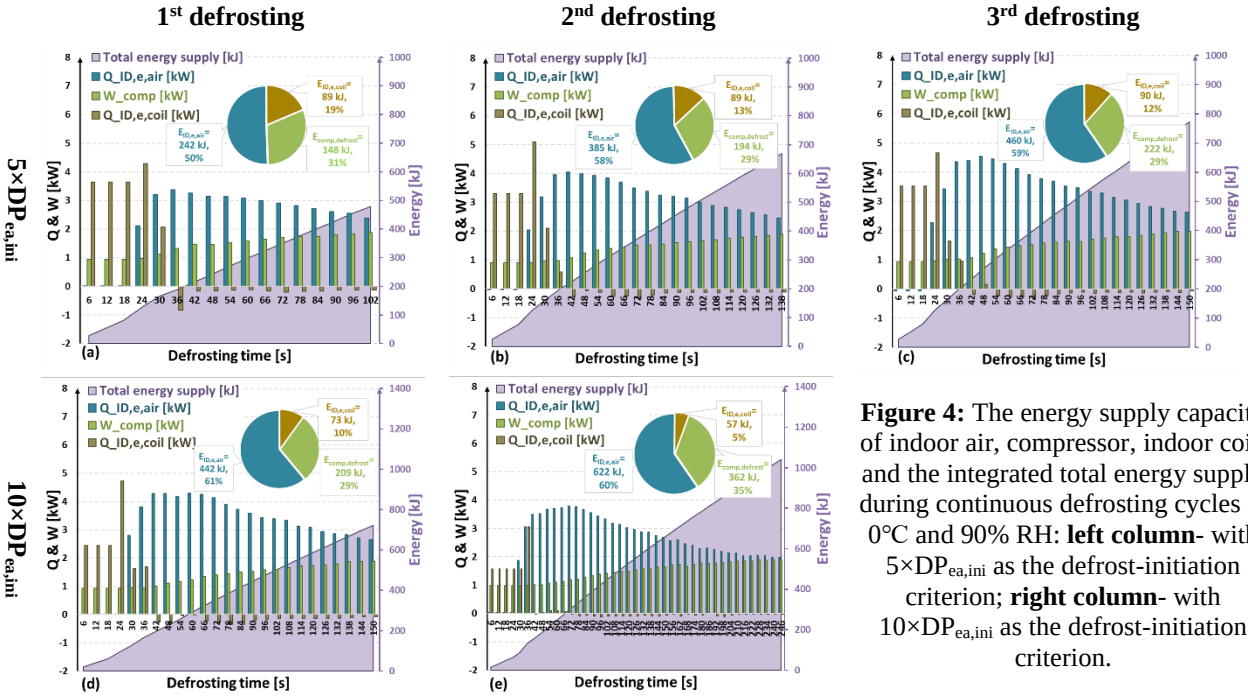

Figure 4: The energy supply capacity of indoor air, compressor, indoor coil, and the integrated total energy supply during continuous defrosting cycles at 0°C and 90% RH: **left column**- with $5\times DP_{ea,ini}$ as the defrost-initiation criterion; **right column**- with $10\times DP_{ea,ini}$ as the defrost-initiation criterion.

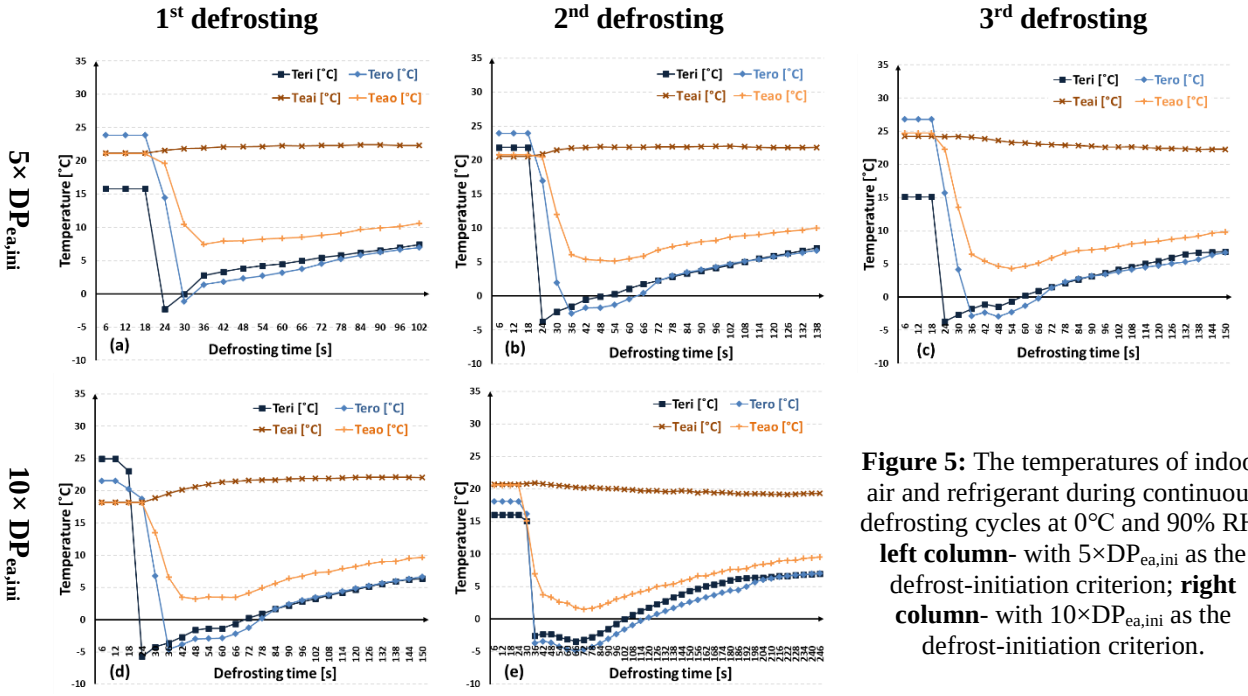

Figure 5: The temperatures of indoor air and refrigerant during continuous defrosting cycles at 0°C and 90% RH: **left column**- with $5\times DP_{ea,ini}$ as the defrost-initiation criterion; **right column**- with $10\times DP_{ea,ini}$ as the defrost-initiation criterion.

Figure 4(a) to (c) show the periodic performance of three defrosting energy sources with 5 times the initial DP_{ea} as the defrost-initiation criterion. The defrosting time is 102, 138, and 150 s, and the total energy supply $E_{total,supply}$ is 479, 669, and 773 kJ for the continuous three defrosting cycles. The total energy supply $E_{total,supply}$ is increasing linearly with the defrosting time $t_{defrosting}$. For the three energy sources, the heat provided by the indoor coil $E_{ID,e,coil}$ is

almost constant to be 90 kJ for the continuous three defrosting cycles. However, the heat provided by the indoor air $E_{ID,e,air,}$ and the energy supplied by the compressor $E_{comp,defrost}$ are increasing proportionally with the defrosting time. $E_{ID,e,air}$ is 242, 385,460 kJ and $E_{comp,defrost}$ is 148, 194, and 222 kJ for the continuous three defrosting cycles. Especially, $E_{ID,e,air}$ increases faster than $E_{comp,defrost}$ with the defrosting time, so the percentage of $E_{ID,e,air}$ out of the total energy supply increases from 50% to 58% from the first to the third defrosting cycle. The higher percentage of $E_{ID,e,air}$ indicates more negative impacts on the indoor temperature: As shown in Figure 5, the minimal air exit temperature T_{eao} was 7.4, 5.1, and 4.3℃ for the continuous three defrosting processes.

By comparing Figure 4(a) and (d), the defrosting time is 47.1% longer and the total energy supply is 50.9% higher for the first defrosting cycle using 10 times than using 5 times of the initial DP_{ea} as the defrost-initiation criterion. The indoor coil provides less heat (73 kJ) when using 10 times the initial DP_{ea} as the defrost-initiation criterion than 5 times. This is due to the longer operating time in the previous frosting cycle, the heating capacity of the indoor gas cooler drops more, and the average temperature of the indoor coil is lower when applying 10 times than 5 times of the initial DP_{ea} as the defrost-initiation criterion. In addition, the sum of the total energy supplied in the three continuous defrosting cycles using 5 times the initial DP_{ea} as the defrost-initiation criterion can be calculated and divided by the total operating time of the HP system: the time-averaged energy supply for defrosting is 20.76 kJ/min. Similarly, it is 15.14 kJ/min for the two continuous defrosting cycles using 10 times the initial DP_{ea} as the defrost-initiation criterion. Thus, it is more energy-efficiently to apply 10 times the initial DP_{ea} as the defrost-initiation criterion.

3.3 The energy consumption during continuous defrosting cycles

Figure 6 shows the heating capacity of the outdoor coil based on refrigerant-side measurements $Q_{OD,c,ref}$ and the integrated total defrosting energy consumption $E_{OD,c,ref}$. Figure 7 presents the four estimated heating loads ($Q_{OD,c,frost,}$ $Q_{OD,c,coil,}$ $Q_{OD,c,water,}$ $Q_{OD,c,loss}$) and the integrated total energy consumption of those four loads. For the accuracy of energy calculation, it can be noticed that integrated total defrosting energy consumption calculated using refrigerant measurements $E_{OD,c,ref}$ in Figure 6 agrees well with the integrated total energy supply $E_{total,supply}$ in Figure 4 for all defrosting experiments (within -4% to 8%). This indicates a good energy balance between independent measurements. However, $E_{OD,c,water}$ is overestimated in Figure 7 (a) and (b), and the integrated total energy consumption of all four terms ($Q_{OD,c,frost,}$ $Q_{OD,c,coil,}$ $Q_{OD,c,water,}$ $Q_{OD,c,loss}$) in Figure 7 (a) and (b) is higher than $E_{OD,c,ref}$ by 57% and 7% for the first and second defrosting cycles using 5 times of the initial DP_{ea} as defrosting criterion. This is due to the imperfectness of water collecting methods and mass measurements in the first few defrosting cycles, as mentioned in the data reduction section. In addition, the heating capacity $Q_{OD,c,ref}$ is not necessarily matching the sum of the four heating loads for each moment during the defrosting since there can be a time delay during the transfer of the energy.

In the first half of defrosting, the heating capacity of outdoor condenser $Q_{OD,c,ref}$ is higher than it is in the latter half (Figure 6). This is due to the low temperature of the outdoor coil metal and the frost at the beginning of defrosting, which leads to a low refrigerant exit temperature T_{cro} and a high heating capacity $Q_{OD,c,ref}$. Also, most of the energy is used to warm the outdoor coil metal and to melt the frost on the outdoor coil in the first half of defrosting, as shown by the brown ($Q_{OD,c,coil}$) and red ($Q_{OD,c,frost}$) columns in Figure 7. This matches the observation that all frost melt in the first 20 to 35 seconds based on the images taken with the webcams. However, as the temperature of the coil metal and the retained water are rising above the critical temperature of CO_2, refrigerant leaves the outdoor coil as superheated vapor or supercritical CO_2. Thus, the heating capacity $Q_{OD,c,ref}$ drops significantly from 7 to 2 kW by the end of each defrosting cycle (Figure 6), even the refrigerant mass flow rate increases slightly. In addition, heat loss $Q_{OD,c,loss}$ increases proportionally to the surface temperature during the defrosting process, and $Q_{OD,c,water}$ rises significantly after the surface temperature is above 50℃, as shown by the orange and yellow columns in Figure 7.

The total energy consumption $E_{OD,c,ref}$ increases linearly with the defrosting time during continuous defrosting cycles. It is 489, 662, and 718 kJ for the three defrosting cycles with 5 times of initial DP_{ea} as the defrost-initiation criterion (Figure 6(a) to (c)), and it is 731 and 1054 kJ for the two defrosting cycles with 10 times of initial DP_{ea} as defrost-initiation criterion (Figure 6(d) to (e)). Although the defrosting time is longer, and the total energy consumption is higher for each defrosting cycle using 10 times the initial DP_{ea} as the defrost-initiation criterion than it is for 5 times (e.g., comparing Figure 6(a) and (d)). But considering the longer operating time in HP mode and fewer defrosting cycles, the time-averaged energy consumption (the sum of $E_{OD,c,ref}$/operating time of HP) is 20.21 and 15.32 kJ/min for using 5 times and 10 times of the initial DP_{ea} as the defrost-initiation criterion. Again, it is more energy-efficiently to apply 10 times the initial DP_{ea} as the defrost-initiation criterion.

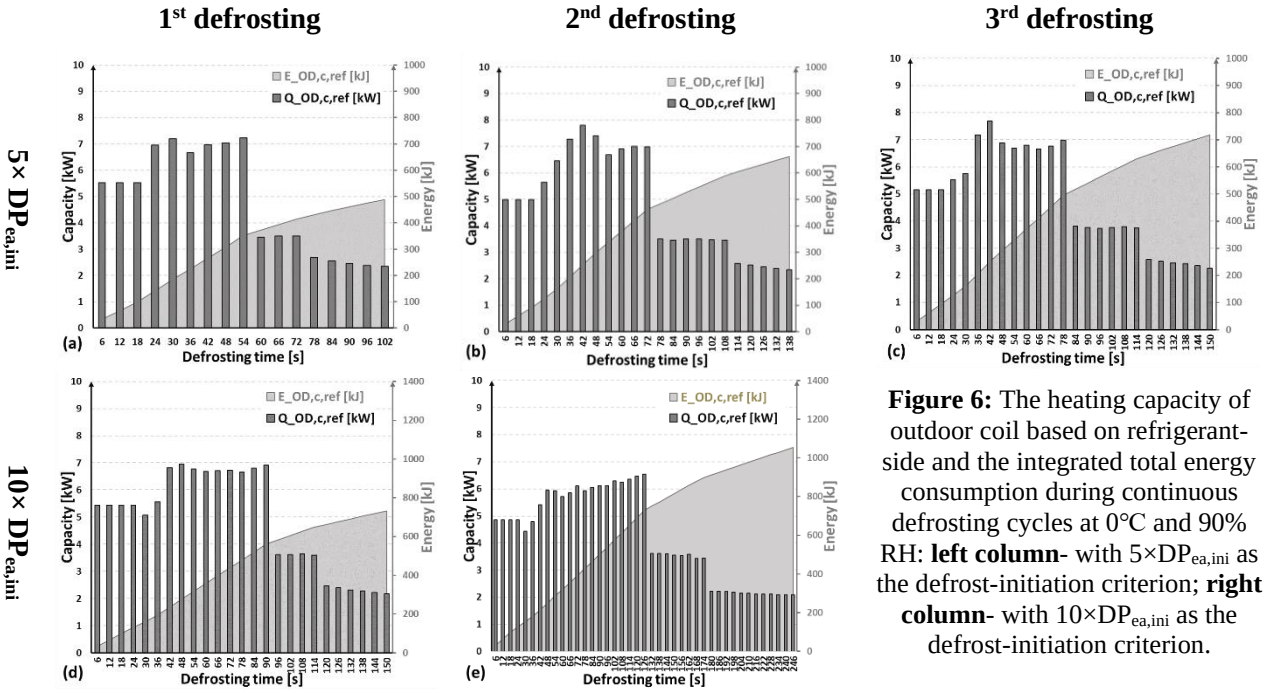

Figure 6: The heating capacity of outdoor coil based on refrigerant-side and the integrated total energy consumption during continuous defrosting cycles at 0°C and 90% RH: **left column**- with 5×$DP_{ea,ini}$ as the defrost-initiation criterion; **right column**- with 10×$DP_{ea,ini}$ as the defrost-initiation criterion.

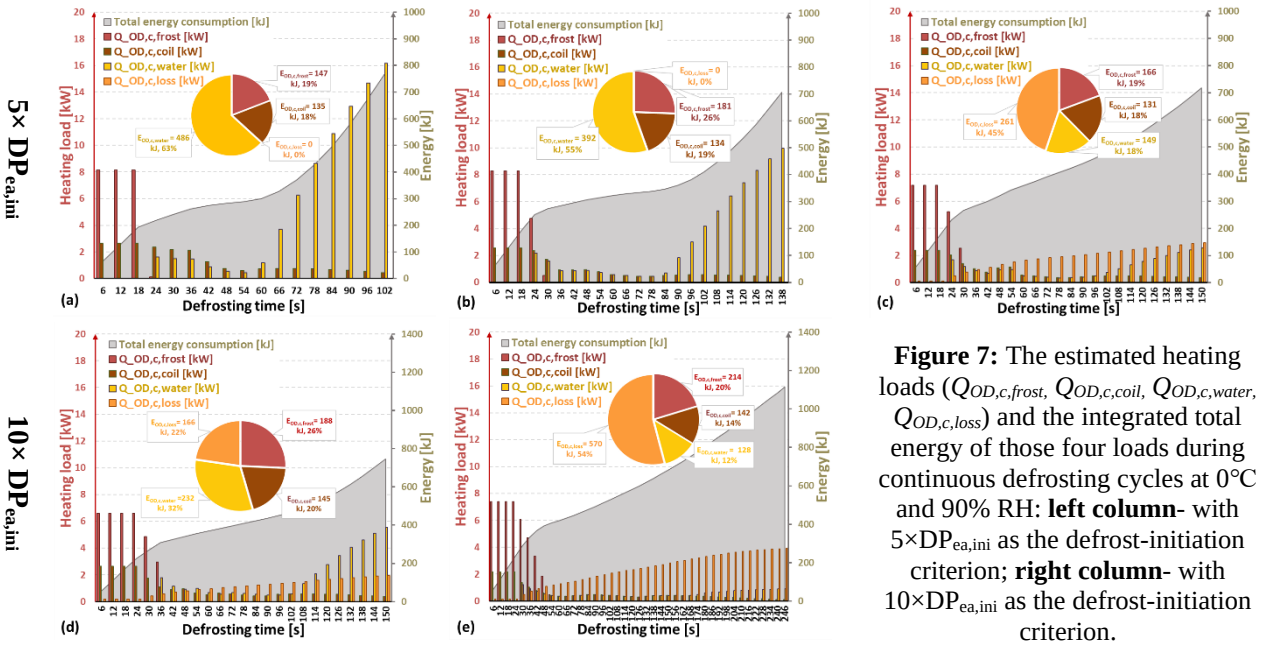

Figure 7: The estimated heating loads ($Q_{OD,c,frost}$, $Q_{OD,c,coil}$, $Q_{OD,c,water}$, $Q_{OD,c,loss}$) and the integrated total energy of those four loads during continuous defrosting cycles at 0°C and 90% RH: **left column**- with 5×$DP_{ea,ini}$ as the defrost-initiation criterion; **right column**- with 10×$DP_{ea,ini}$ as the defrost-initiation criterion.

4. CONCLUSIONS

In this paper, we investigated the energy flow during the continuous defrosting cycles with a transcritical CO_2 system in the outdoor condition of 0°C and 90% RH. The results show:

- The defrosting time $t_{defrosting}$ and water retention $M_{retained}$ on the outdoor coil increase with the number of the frosting/defrosting cycles due to the formation of ice in the next cycle. On the contrary, $M_{vaporized}$ reduces with the increased number of the frosting/defrosting cycles (Figure 2) due to the increased thickness of the water film and lower temperature of the water-air interface.

- $E_{ID,e,coil}$ is almost constant to be 90 kJ for the continuous three defrosting cycles (with 5 times $DP_{ea,ini}$). But the $E_{ID,e,air}$ and $E_{comp,defrost}$ are increasing proportionally with the defrosting time $t_{defrosting}$.

- It is more energy-efficient to extend the operating time in HP mode and apply 10 times the initial DP_{ea} as the defrost-initiation criterion.

NOMENCLATURE

AC	air-conditioning	**IHX**	internal heat exchanger
Acc	accumulator	**M**	mass [kg]
COP	Coefficient of Performance	**P**	pressure [bar]
DP	differential pressure [Pa]	**Q**	capacity [kW]
EXV	electronic expansion valve	**T**	temperature [℃]
h	enthalpy [kJ/kg-℃]	**V**	velocity [m/s]
HP	heat pump	**W**	power [kW]
HPF	Heating Performance Factor		
Subscript			
a/ air	air-side	i	inlet
acc	accumulator	g	glycol
c	Condenser/ gas cooler	n	nozzle
cp/ comp	compressor	o	outlet
e	evaporator	r/ ref	refrigerant-side
elec	electricity	x	expansion valve
high	high-pressure side		

REFERENCES

Dong, J., Deng, S., Jiang, Y., Xia, L., & Yao, Y. (2012). An experimental study on defrosting heat supplies and energy consumptions during a reverse cycle defrost operation for an air source heat pump. *Applied Thermal Engineering*, *37*, 380–387. https://doi.org/10.1016/j.applthermaleng.2011.11.052

Huang, D., Li, Q., & Yuan, X. (2009). Comparison between hot-gas bypass defrosting and reverse-cycle defrosting methods on an air-to-water heat pump. *Applied Energy*, *86*(9), 1697–1703. https://doi.org/10.1016/j.apenergy.2008.11.023

Payne, V., & O'neal, D. L. (1995). Defrost cycle performance for an air-source heat pump with a scroll and a reciprocating compressor. *International Journal of Refrigeration*, *18*(2), 107–112. https://doi.org/10.1016/0140-7007(95)93893-O

Song, M., Xu, X., Mao, N., Deng, S., & Xu, Y. (2017). Energy transfer procession in an air source heat pump unit during defrosting. *Applied Energy*, *204*, 679–689. https://doi.org/10.1016/j.apenergy.2017.07.063

Steiner, A., & Rieberer, R. (2013). Parametric analysis of the defrosting process of a reversible heat pump system for electric vehicles. *Applied Thermal Engineering*, *61*(2), 393–400. https://doi.org/10.1016/j.applthermaleng.2013.07.044

Zhang, W., & Hrnjak, P. (2021). The performance of an automotive carbon dioxide heat pump system in frosting and defrosting. *18th International Refrigeration and Air Conditioning Conference at Purdue*. Paper 2111. https://docs.lib.purdue.edu/iracc/2111

ACKNOWLEDGEMENT

This work was supported by all members of ACRC at the University of Illinois at Urbana-Champaign. All the help from our members is gratefully acknowledged!